Article

Causes and multiyear predictability of the rapid acceleration of U.S. Southeast Sea level rise after 2010

Check for updates

Liping Zhang [1,2] ✉, Thomas L. Delworth [1], Xiaosong Yang [1], Fanrong Zeng[1], Qinxue Gu[1,3] & Shouwei Li[1,3]

The rate of sea level rise (SLR) along the Southeast Coast of the U.S. increased significantly after 2010. While anthropogenic radiative forcing causes an acceleration of global mean SLR, regional changes in the rate of SLR are strongly influenced by internal variability. Here we use observations and climate models to show that the rapid increase in the rate of SLR along the U.S. Southeast Coast after 2010 is due in part to multidecadal buoyancy-driven Atlantic meridional overturning circulation (AMOC) variations, along with heat transport convergence from wind-driven ocean circulation changes. We show that an initialized decadal prediction system can provide skillful regional SLR predictions induced by AMOC variations 5 years in advance, while wind-driven sea level variations are predictable 2 years in advance. Our results suggest that the rate of coastal SLR and its associated flooding risk along the U.S. southeastern seaboard are potentially predictable on multiyear timescales.

Sea level rise (SLR) is one of the most severe consequences of a warming climate, causing dangerous flooding and therefore threatening lives and infrastructure in low-lying coastal regions[1–3]. Coastal sea level fluctuations vary on a broad range of time scales, from hours to centuries[4–9]. The low frequency SLR provide a background state, modulating the effect of high frequency synoptic weather events and tides[10,11]. The superposition of short term SLR induced by storms and hurricanes on top of decadal and longer SLR can produce extreme sea level events with devastating socioeconomic consequences[4]. In a changing climate, both external radiative forcing and internal variability influence SLR across a range of timescales[12].

In the most recent decade, the U.S. Southeast Coast (USSEC) was identified as a "hot spot" for rapid SLR in the North Atlantic (NA) Ocean[12–18] (Fig. 1a, b). The linear trend of SLR along the USSEC in 2010–2022 in observations is ~10.8 mm/year, which is 3–4 times larger than that in 1920–2009 (~ 2.6 mm/year). This is in stark contrast to a weak deceleration of SLR after 2010 that occurred north of Cape Hatteras (Fig. 1a). Several hypotheses have been proposed to explain this rapid acceleration. A leading idea involves changes in the strength/position of the Gulf Stream (GS) system and the Atlantic meridional overturning circulation (AMOC)[12,17,18]. Another explanation involves warming of the Florida current/GS waters[15], or the large-scale heat convergence in the NA subtropical gyre related to the North Atlantic Oscillation (NAO)[13]. A recent study suggested that this SLR acceleration reflected the combined effects of external forcing and wind driven Rossby waves in the tropical NA[12]. Atmosphere condition changes

also affected the sea levels over the USSEC via the inverse barometer effect[16]. Overall, processes and mechanisms causing the rapid acceleration of SLR along the USSEC are still under debate.

The accelerated SLR over the densely populated USSEC could elevate storm surge and exacerbate coastal flooding when it coincides with record-breaking NA hurricane seasons[4–6]. Thus, there is a pressing need to understand and predict this rapid acceleration of SLR to assist in mitigating and adapting to SLR impacts. In this study, we combine observations[19,20] and model simulations to explore the mechanisms and multiyear predictability of sea level along the USSEC. We use both reanalysis and initialized decadal predictions using the Geophysical Fluid Dynamics Laboratory (GFDL) developed SPEAR[21] modeling system. We find that the accelerated SLR after 2010 represents the compounding effects of long-term global warming trend, buoyancy-driven AMOC variations and wind-driven tripole-like response in sea level to variations in the NAO. We show that an initialized decadal prediction system can provide skillful regional SLR predictions induced by buoyancy-driven AMOC variations 5 years in advance, while wind-driven sea level variations are predictable 2 years in advance.

Results

NA sea level tripole during the satellite era

It is well known that global warming tends to increase sea level over most oceans due to thermal expansion and the melting of land ice[22–25]. Here we argue that the accelerated SLR along the USSEC in the most recent decade is

[1]NOAA/Geophysical Fluid Dynamics Laboratory, Princeton, NJ, USA. [2]University Corporation for Atmospheric Research, Boulder, CO, USA. [3]The Program in Atmospheric and Oceanic Sciences, Princeton Abduversity, Princeton, NJ, USA. ✉e-mail: Liping.Zhang@noaa.gov
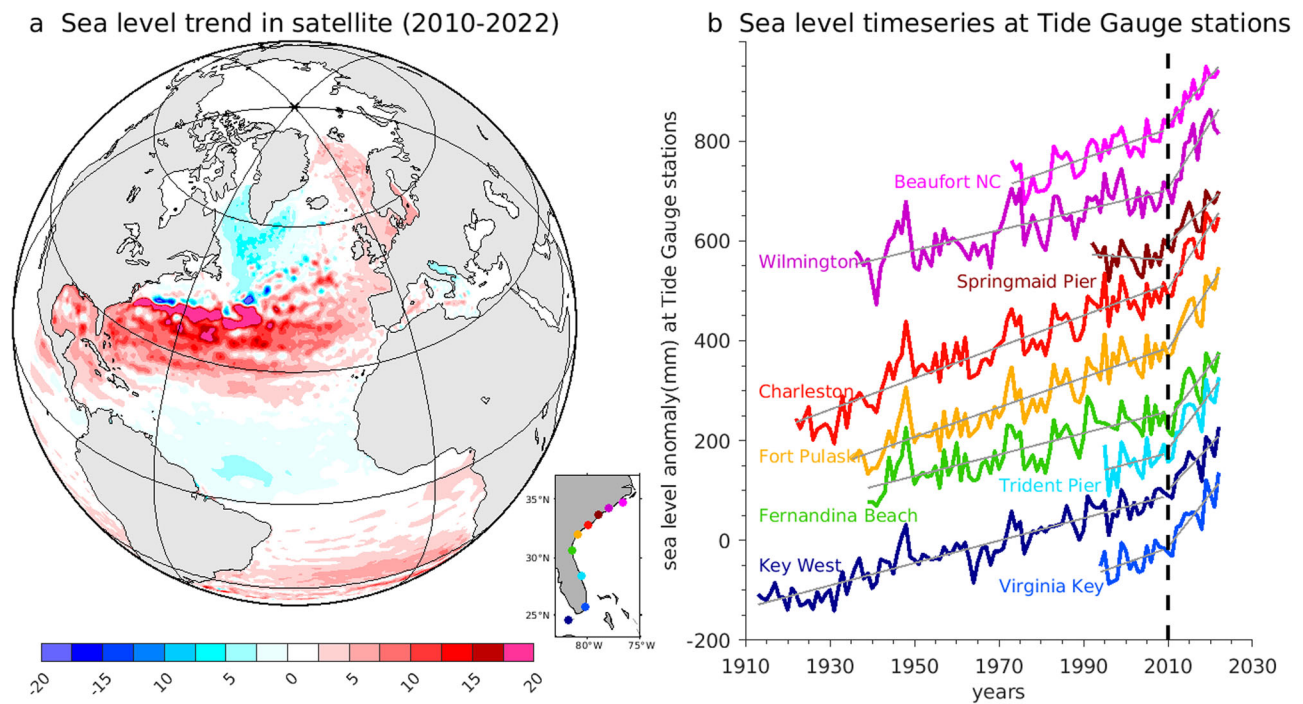
Fig. 1 | Rapid acceleration of sea level rise after 2010 in observations. a The linear trend of sea level (mm/year) in 2010–2022 in satellite observation. **b** Time series of annual mean sea level anomaly (mm) at various Tide Gauge (TG) stations along the U.S. Southeast Coast. Rainbow dots in the bottom-left subplot denotes the locations of TG stations. The solid grey lines in (**b**) denote the linear trend of sea level prior to and after 2010 at various Tide Gauge stations. Constant values have been added to each of the time series in (**b**) to provide offsets for visual clarity. The values added to the time series, going from south to north, are (in mm): 0, 0, 200, 200, 300, 400, 600, 650, and 800.

the result of a compounding effect arising from long-term global warming trend and the NA sea level tripole. The leading empirical orthogonal function (EOF) mode of detrended sea level (see "Methods") in the NA Ocean in satellite observation is characterized by a tripole pattern[13,26], with sea level anomalies of one sign over the subtropical band (15°–40°N) and anomalies of the opposite sign in the subpolar and tropical regions (Fig. 2a). The maximum sea level variability occurs near the GS and its extension regions. This tripole pattern imprints itself on the U.S. east coast, manifested as an out of phase sea level variability to the north and south of Cape Hatteras. The time evolution of the tripole sea level pattern exhibits pronounced interannual to decadal-scale variability (Fig. 2d). There is an extreme low value in 2010, coincident with a strongly negative NAO and the weakest AMOC state at 26.5°N in observation[27,28]. From 2010 to 2022, the timeseries shows a strong upward trend, indicating that this sea level tripole plays a crucial role in the accelerated SLR over the USSEC in the most recent decade.

The SPEAR reanalysis (partially constrained by observations, see "Methods") realistically reproduces the observed sea level tripole with a maximum variability near the GS path (Fig. 2b, d), although the reanalysis displays some discontinuities south of 40°N. The temporal evolution of the tripole in reanalysis also agrees well with observation (Fig. 2d). In both observation and reanalysis, the sea level tripole is accompanied with a positive NAO-like atmosphere circulation (Fig. 2a, b), with high sea levels corresponding to high (low) sea level pressures (SLPs) over the subtropical (subpolar) region. However, the maximum SLP centers are not collocated with the maximum sea level variability regions. This mismatch implies that the tripole is not a simple reflection of short time processes such as Ekman pumping but a product of horizontal or meridional circulation adjustments.

In the SPEAR control simulation (see "Methods"), we see a similar sea level tripole as in observations and reanalysis (Fig. 2a–c). The tripole structure and strong sea level variability near the GS path are well retained in the control run. However, the simulated sea level variability over the subtropical interior ocean and Gulf of Mexico is much weaker than that in

observation and reanalysis. The tripole timeseries in the control run exhibits pronounced decadal to multidecadal variability, with a spectral peak around 35 years (Fig. 2e). This multidecadal period is similar to the timescale of internal buoyancy-driven AMOC variations in the control simulation as shown in previous paper[29,30], suggesting a potential linkage between the sea level tripole and AMOC variations. To verify this speculation, we regress the Atlantic streamfunction against the sea level timeseries. As displayed in Fig. 2g, the tripole corresponds to streamfunction anomalies of one sign in the subpolar subsurface ocean that extend southward along the deep ocean and streamfunction anomalies of the opposite sign from 200 to 2500 m in the Atlantic south of 40°N (Fig. 2g). This streamfunction pattern strongly resembles the transition phase of internal AMOC variability, when the AMOC transitions from its negative phase to its positive phase (Supplementary Fig. 1, Lags = 4, 8 years). This suggests that the sea level tripole in control run is a fingerprint of the AMOC adjustment[29]. We find a very similar streamfunction pattern in the SPEAR reanalysis (Fig. 2f versus Fig. 2g). This similarity implies that the buoyancy-driven AMOC variation plays a crucial role in the accelerated SLR after 2010 in reanalysis and observation, particularly near the GS path and USSEC.

Nevertheless, the difference in the tripole pattern between the SPEAR control run and reanalysis suggests that the accelerated SLR in the subtropical band, as observed, cannot be solely attributed to AMOC adjustment. As described below, we find that the positive NAO-like winds are also critical for the SLR acceleration. As shown in Fig. 2a–c, the NAO-like wind associated with the tripole in SPEAR reanalysis and observation is much stronger than that in the control simulation. To evaluate the role of such wind stress changes in the increased rate of SLR over the NA, we conduct simulations using SPEAR in which we prescribe these wind stress differences between observation/reanalysis and control run in our coupled SPEAR model and integrate the model for 8 years (Supplementary Fig. 2). The results show that the positive NAO-like wind stress drives high sea level over the whole subtropical region, including the interior ocean, USSEC and Gulf of Mexico. By comparing the satellite observation, SPEAR reanalysis,
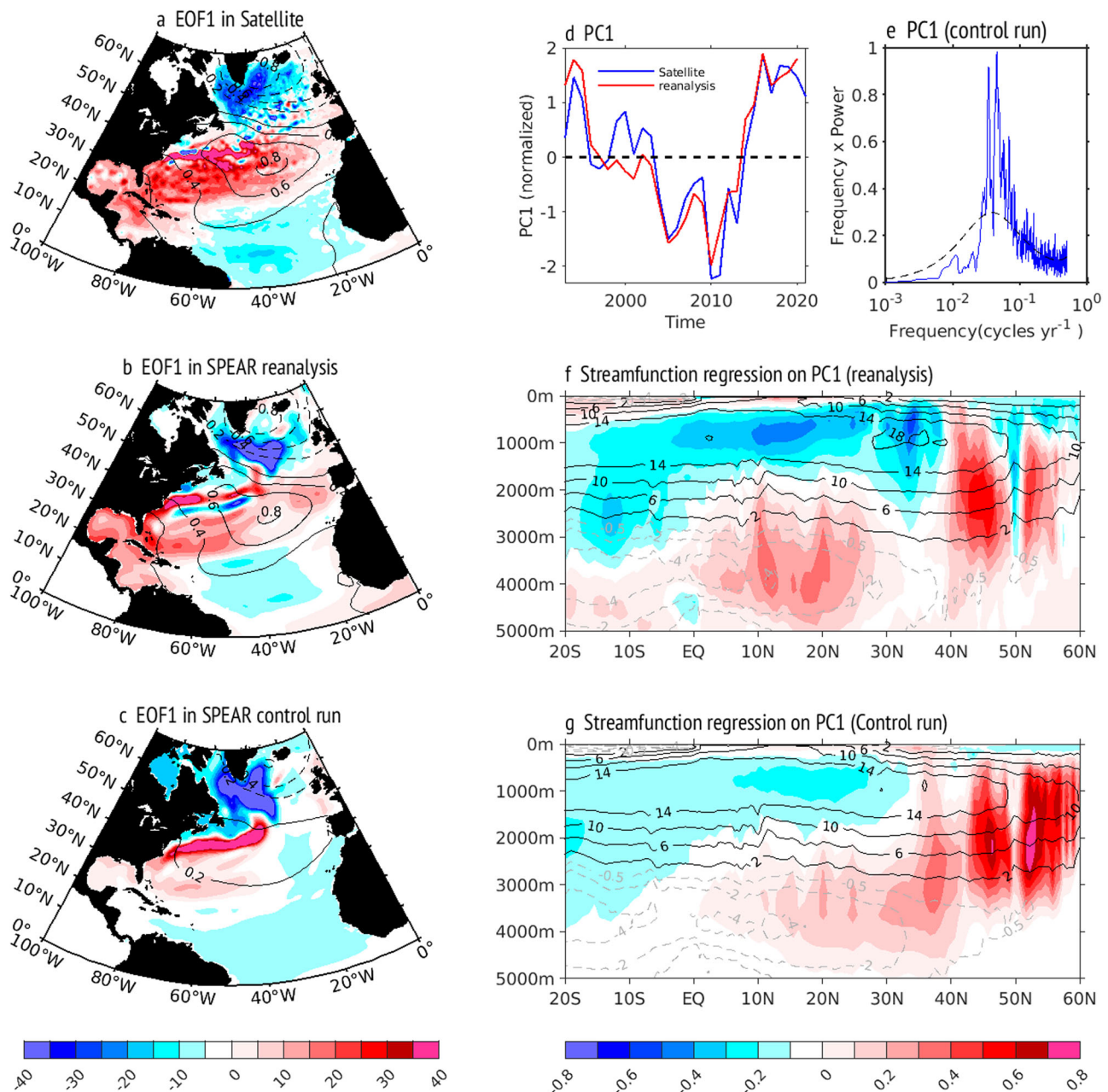
Fig. 2 | The North Atlantic sea level tripole mode in satellite observation, SPEAR reanalysis and control run. a The leading empirical orthogonal function (EOF1) of detrended sea level in satellite observation (1993-present). **b** The EOF1 of detrended sea level in SPEAR reanalysis since the satellite era. **c** The EOF1 of sea level in SPEAR control simulation. The contours in (**a–c**) are the sea level pressure (SLP) regressions upon the sea level EOF1 timeseries. **d** The first principal component (PC1) of sea level in satellite observation (blue line) and SPEAR reanalysis (red line). **e** Power spectrum of the PC1 of sea level in SPEAR control simulation. **f** Regression of Atlantic streamfunction against the sea level timeseries in SPEAR reanalysis (shading). The contours denote the long term mean Atlantic meridional overturning circulation (AMOC) state. **g** Same as (**f**) but for the SPEAR control run. The units for the sea level EOF1, PC1, SLP regression and the Atlantic streamfunction regression are mm, 1, hPa and Sv, respectively.

control run, and sensitivity run, we conclude that the buoyancy-driven AMOC and the NAO-like wind-driven circulation adjustments mutually contribute to the observed SLR acceleration along the USSEC.

The wind-driven circulation adjustment is further seen in the EOF analysis of SPEAR control simulation (Fig. 3). We use a 15-year low pass filter to separate the sea level variability into two bands: low frequency variability (> = 15-year) and high frequency variability (<15-year). The total sea level variability is dominated by a low frequency component (Fig. 2c, e; Fig. 3a) that reflects the AMOC fingerprint (Fig. 2g) with weak surface wind response (Fig. 2c, Fig. 3b). The high frequency component corresponds to a strong NAO-like wind response and shows a broad pattern of high sea level

over the whole subtropical band (Fig. 3c, d), in stark contrast to the AMOC fingerprint where there is a narrow sea level band around 40°N. This high frequency tripole sea level component is largely driven by the NAO-like wind and is strongly connected with the NA sea surface temperature (SST) tripole as mentioned by previous studies[31–33].

Mechanisms and predictability of the accelerated NA SLR
We next investigate the processes through which the buoyancy-driven AMOC and wind-driven circulation could affect sea level near the USSEC. It is found that the accelerated SLR in the NA Ocean in the SPEAR reanalysis is primarily due to meridional heat transport convergence associated with the
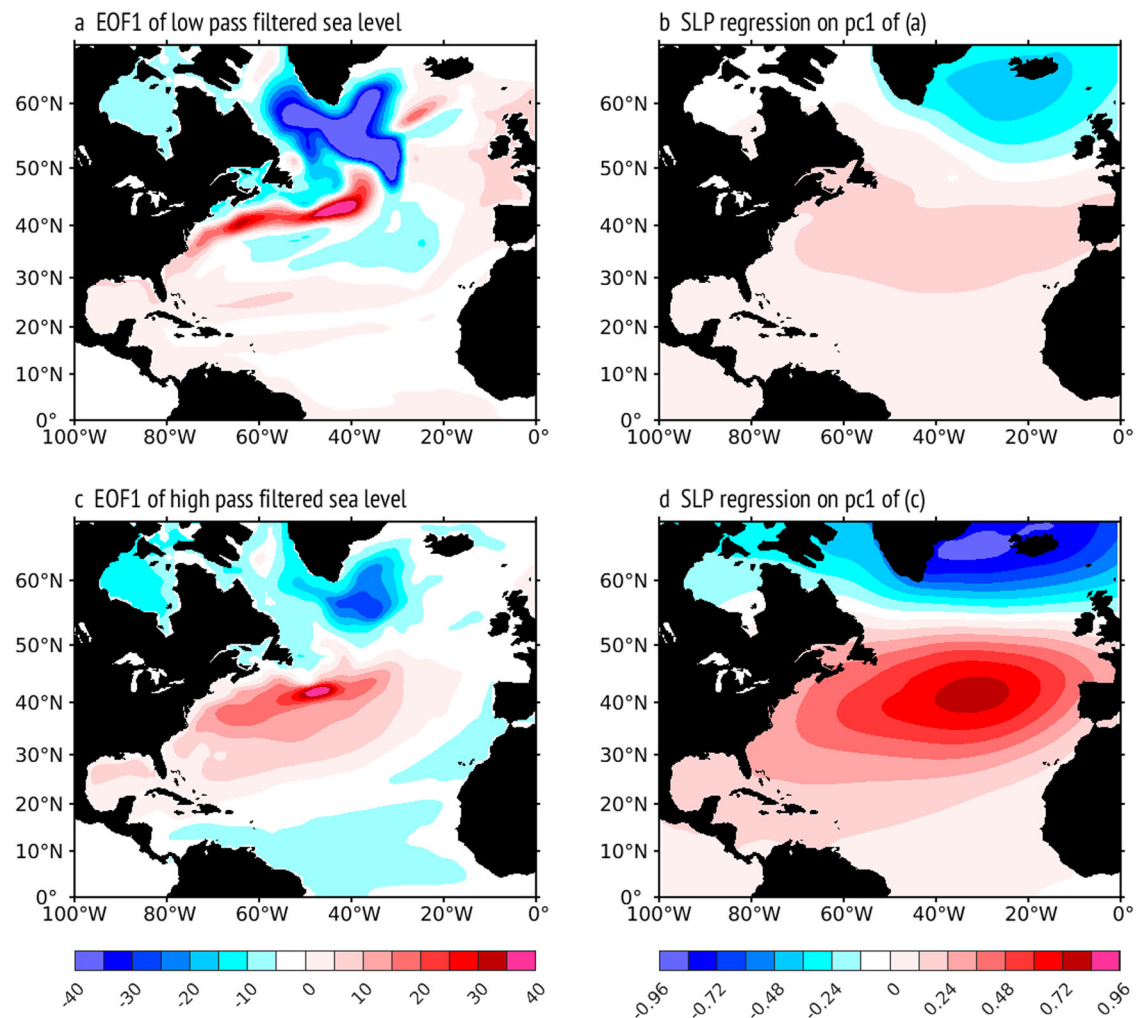
Fig. 3 | The empirical orthogonal function (EOF) of low/high pass filtered North Atlantic (NA) sea level anomalies in the SPEAR control simulation. a The first EOF (EOF1) spatial pattern of low-pass filtered (> = 15 years) NA sea level variability. **b** Regression of the sea level pressure (SLP) anomalies against the first principal component (PC1) of low-pass filtered sea level timeseries. **c, d** Same as (**a, b**) but for the high-pass filtered sea level variability (< 15 years). Units are mm for the sea level spatial pattern and hPa for the SLP regressions. The filtering is based on the fast Fourier transform and inverse fast Fourier transform methods.

circulation adjustments (Fig. 4a–c), in agreement with the observational analysis[13]. The accelerated SLR in the subtropical band largely arises from the steric component (see "Methods"), particularly the thermosteric component (Fig. 4a, b). The halosteric sea level component contributes very little, only partially compensating the thermosteric component (not shown). The high sea levels due to steric effect in the subtropical gyre and Gulf Stream regions further extend to the USSEC due to ocean mass redistribution[22]. A close examination finds that the monthly time derivatives of sea level averaged in the subtropical band are positively correlated (correlation = 0.62, P-value < 0.01) and of the same magnitude with the meridional heat transport convergence/divergence within 25°–45°N (Supplementary Fig. 3), suggesting that the heat convergence is a main driver for the SLR acceleration according to the thermosteric sea level equation (see "Methods"). We also display in Fig. 4c the regression of meridional heat transport convergence/divergence against the monthly time derivatives of the tripole time series. It further confirms that the heat transport convergence in the subtropical band leads to a warming and thus high sea levels in the subtropical band and vice versa for the subpolar region.

The buoyancy-driven AMOC's role in the heat transport convergence and therefore SLR is clearly seen from the SPEAR control simulation. Like the reanalysis, the positive sea levels near the GS path in the control run are largely contributed from the thermosteric component (Fig. 5a–c). When the AMOC transitions from a peak negative phase to a positive phase, the weak

AMOC anomalies propagate southward with a slow advection speed due to the existence of the interior pathway of North Atlantic deep water[34,35] (Fig. 5d), which is accompanied with a northward shift of GS path (Fig. 5a). The associated northward heat transport anomalies lead to a heat convergence near the GS path, thus warming and elevating sea levels nearby the GS path (Fig. 5e, f). The opposite occurs in the subpolar gyre region. In the meantime, the high/low SLP associated with the positive NAO-like wind (Fig. 2a, b) favors a heat transport convergence (divergence) in the subtropical (subpolar) region through Ekman transport and ocean circulations, which positively facilitates the effect of the buoyancy-driven AMOC adjustment. The wind driven meridional cell, such as the AMOC at 26.5°N, converges heat in the subtropical band[13,26]. The negative wind stress curl anomalies also spin up the subtropical gyre, converge heat in the interior ocean and western boundary, elevating the sea level in the entire subtropical band.

Given the important role of buoyancy-driven AMOC changes in the accelerated SLR in the NA Ocean, we explore if the long-time scales associated with the AMOC variability would lead to predictability of sea level in the USSEC. We investigate this by comparing the SPEAR initialized decadal hindcasts[21] (See "Methods") and Tide Gauge (TG) observations[20]. The detrended sea level timeseries at TG stations along the USSEC are highly correlated with satellite observation, displaying a robust SLR after 2010 (Figs. 2d, 4d). The initialized hindcasts at lead times from 1 to 5 years successfully capture this rising trend from 2010–2022. The correlation
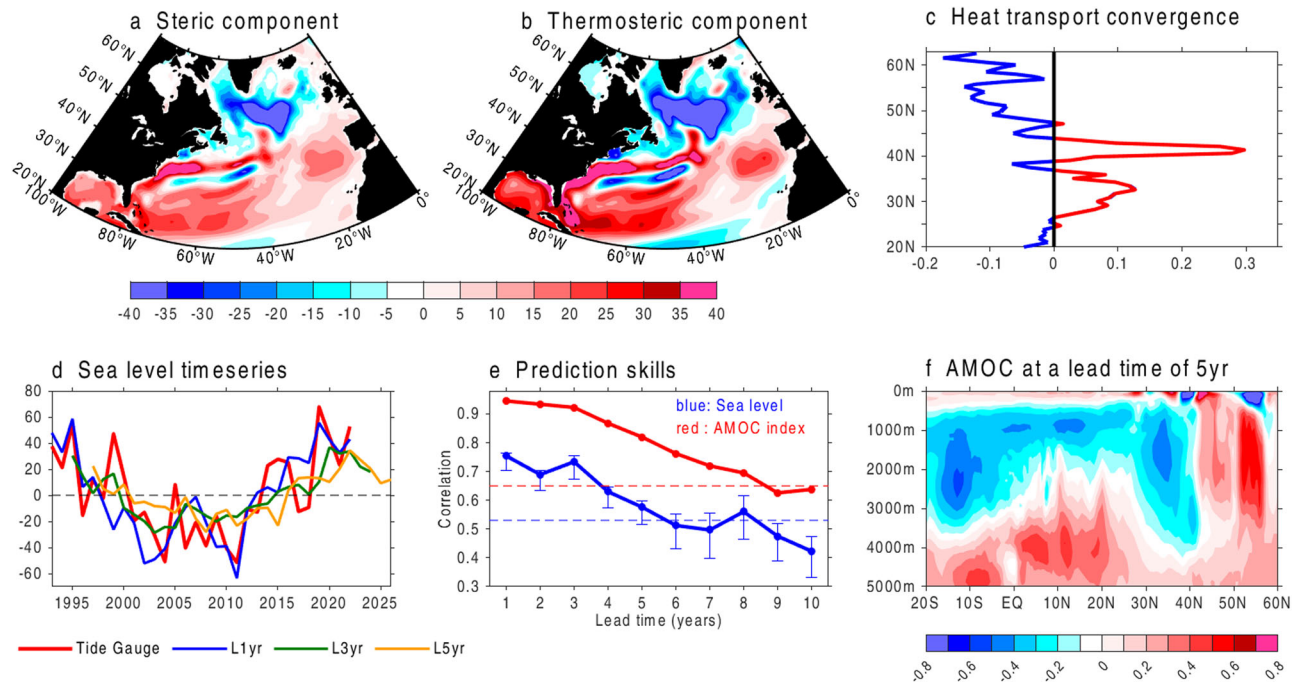
Fig. 4 | Processes and predictability of the North Atlantic (NA) sea level during the satellite era. a Regression of the NA steric sea level component against the sea level PC1 timeseries in SPEAR reanalysis shown in Fig. 2d. **b** Same as (**a**) but for the thermosteric sea level component regression. Unit is mm. **c** Regression of the meridional heat transport convergence (positive/negative denotes heat convergence/divergence) against the time derivatives of monthly PC1 timeseries in SPEAR reanalysis. Unit is PW·month. **d** The composited detrended sea level timeseries at Tide Gauge (TG) stations over the U.S. Southeast Coast (red line) along with the ensemble mean sea level timeseries in the initialized decadal hindcasts at a lead time of 1 year (blue line), 3 years (green line) and 5 years (yellow line). Unit is mm. **e** The anomaly correlation between the detrended ensemble mean sea level timeseries in the initialized decadal hindcasts and detrended TG observations as a

function of lead times (blue solid line). The error bars around the line denote the ensemble spread at each lead time. The dashed blue line denotes the 90% confidence level using a Monte Carlo method (see "methods"). The red solid line denotes the anomaly correlation between the ensemble mean Atlantic meridional overturning circulation (AMOC) index in the initialized decadal hindcasts and the SPEAR reanalysis as a function of lead times. The AMOC index is defined as the maximum streamfunction within 20°–60°N latitudinal band and below 500 m in depth space. The dashed red line denotes the 90% confidence level using a Monte Carlo method. **f** Regression of the Atlantic streamfunction against the EOF1 timeseries of detrended sea level variability at a lead time of 5-year in the initialized decadal hindcasts. Unit is Sv.

coefficients show sea level variations along the USSEC during the satellite era are predictable up to 5 years in advance (Fig. 4e). The successful prediction is largely due to the correct initialization of the observation constrained AMOC state in the model (Fig. 4f). The AMOC state at a lead time of 5 years in the decadal hindcasts highly resembles that in reanalysis (Fig. 2f vs Fig. 4f). As shown in Fig. 4e and a previous study[21], the AMOC in the decadal hindcast can be predicted ~ 8 years in advance when verified by the SPEAR reanalysis. The slow variations of the AMOC and its associated heat transport convergence near the GS path eventually provide a multi-year prediction skill for sea level along the USSEC.

NA sea level variability looking back into the 20th century

The above analysis focuses on the variability of sea level over the most recent three decades, a period for which we have satellite observations. Next, we will broaden our study to encompass a longer time range using the SPEAR reanalysis and TG observations. The EOF analysis of SPEAR reanalysis, covering the period from 1958 to 2022, distinctly identifies sea level variability. It attributes this variability to fluctuations in the buoyancy-driven AMOC (Fig. 6a–d) and wind-driven circulation adjustments (Fig. 6e, f). This finding sharply contrasts with the outcomes observed in the short-term analysis during the satellite era (post-1993), where a mixture of the buoyancy-driven AMOC signal and wind-driven circulation responses is evident, as shown in Fig. 2b and d. We show in Fig. 6a and b the leading EOF mode of detrended sea level over the NA Ocean in the SPEAR reanalysis. The spatial pattern has a maximum loading to the east of Newfoundland that extends to the U.S. Northeast Coast, which corresponds to a mature weak phase of the AMOC when the AMOC anomalies have a maximum negative amplitude (Fig. 7a and Supplementary Fig. 1). The associated

timeseries has a pronounced multidecadal variability, which is out of phase with the AMOC index in the SPEAR reanalysis and in phase with the sea level observations at the U.S. northeast TG stations (Fig. 6b). The negative correlation with the AMOC index is because a weak AMOC is accompanied with a weak GS which leads to a high sea level along the U.S. Northeast Coast as required by the geostrophic balance[22,36]. The agreement between the TG observations and reanalysis along the U.S. Northeast Coast further enhances our confidence on the reliability of SPEAR reanalysis.

The second and third EOF components of sea level in reanalysis are linked to the AMOC transition state (Fig. 6c vs Fig. 7b; Supplementary Fig. 1) and the wind-driven NA tripole mode (Fig. 6e vs Fig. 3c), respectively. Both the spatial pattern of EOF2 and the regressed Atlantic meridional overturning streamfunction pattern against the PC2 (Fig. 6c and Fig. 7b) demonstrate significant similarities with the AMOC transition state during an internal cycle (Lag = 8 years in Supplementary Fig. 1). Again, the NA tripole mode in 1958–2022 is largely associated with the NAO (Fig. 6e) and has substantial variabilities on decadal timescales (Fig. 6f and Fig. 7c). Along the USSEC, the sea level timeseries in reanalysis highly covaries with the TG observations, which reflects a combined product of the second and third EOF modes (Fig. 6g). In the most recent decades, both the AMOC transition state and the NA tripole mode contribute to the rapid SLR after 2010. Prior to 1995, the sea level timeseries have substantial decadal variabilities (Fig. 7d), suggesting a large impact from the NA tripole mode. The detrended sea level timeseries along the USSEC in the initialized hindcasts have a prediction skill up to three years in 1958–2022[36] (Fig. 6g, h). This skill is lower than the sea level skills during the satellite era (~5 years, Fig. 4e), due to less predictable high frequency sea level variabilities prior to 1995. We then show in Fig. 6i the prediction skill of high pass filtered sea level timeseries (< 15-yr)
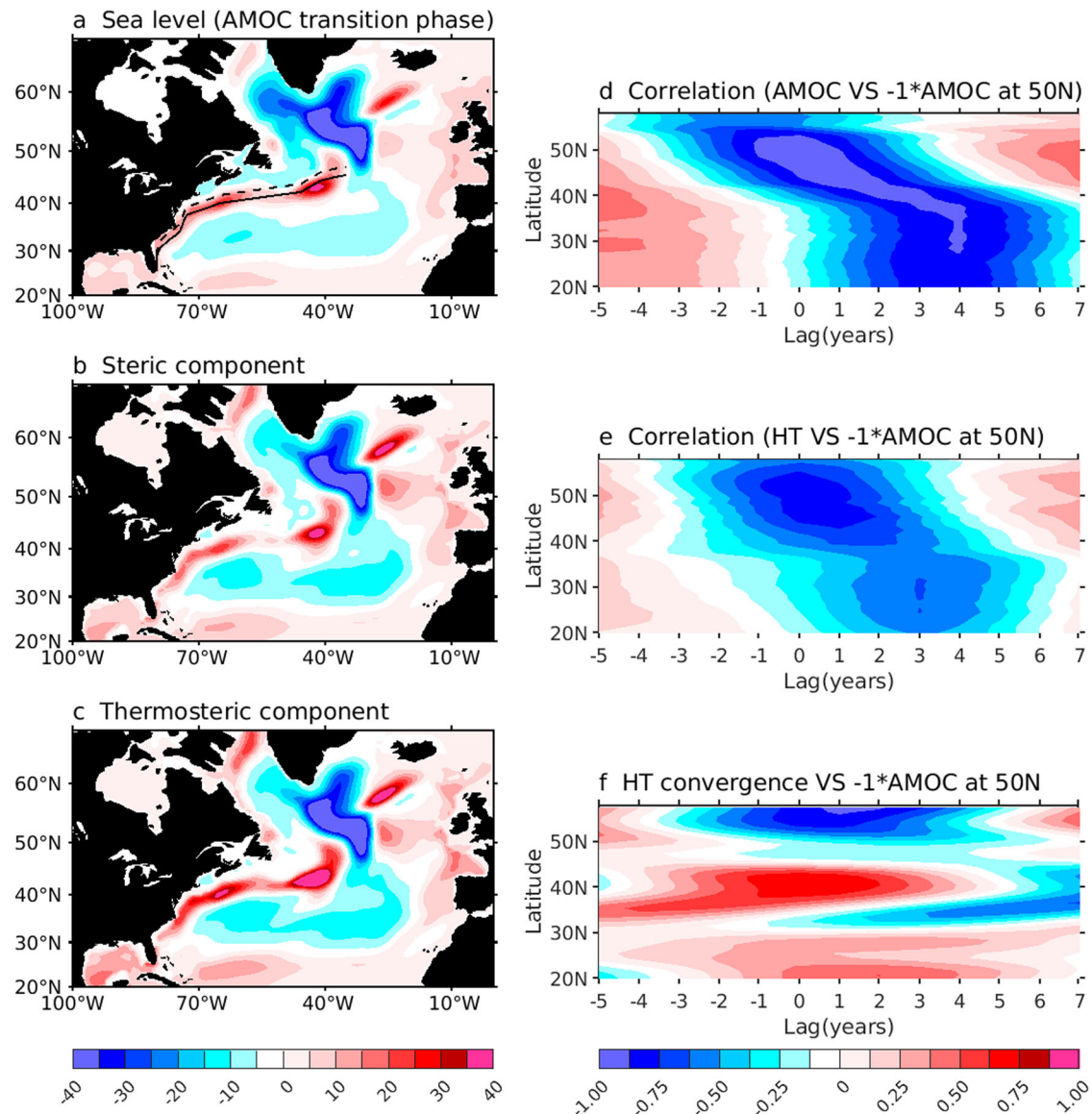
Fig. 5 | North Atlantic (NA) sea level tripole pattern, southward propagation of the Atlantic meridional overturning circulation (AMOC) and its associated heat transport in the SPEAR control simulation. a The spatial pattern of NA sea level associated with the AMOC transition phase, obtained from composite analysis. The AMOC exhibits a ~ 35 years spectrum peak in the control run. The transition state of the AMOC is identified by the time points at which the anomalous AMOC index crosses the zero point from a negative state to a positive state. The corresponding sea levels during these time points are averaged to determine the sea levels during the AMOC transition state. **b** The steric component of NA sea level. **c** The thermosteric component of NA sea level. **d** Lagged correlation of the AMOC anomaly at each latitude with the AMOC anomaly at 50°N in density space multiplied by a factor of −1. At each latitude, the AMOC index is defined as the maximum Atlantic meridional streamfunction value in density space at that specific latitude. **e** Lagged correlation of the meridional heat transport (HT) anomaly at each latitude with the AMOC anomaly at 50°N in density space multiplied by a factor of −1. **f** Lagged correlation of the convergence/divergence of meridional heat transport anomaly at each latitude with the AMOC anomaly at 50°N in density space multiplied by a factor of −1. Units are mm for the sea level and 1 for the correlation. Positive (negative) lags mean the AMOC at 50°N leads (lags) the AMOC/heat transport at other latitudes. The solid black line in (**a**) denotes the long term mean Gulf Stream path in control run. For each latitude, the Gulf Stream path is defined as the longitude where the zonal sea surface height gradient reaches its maximum value. The dashed black line in (**a**) denotes the composited Gulf Stream path when the sea level is during the AMOC transition state.

in 1958–2022. We clearly see that the sea level prediction skill degrades from the original three years to two years.

To explore this two-years predictability source of sea level, we use a diagnostic average predictability time (APT) method[37–39] (see "Methods") to derive the most predictable sea level components in the initialized hindcasts. After removing the predictability associated with global warming trend and buoyancy-driven AMOC variabilities shown in our previous paper[36] (also see "Methods"), the most predictable sea level component is characterized by a tripole pattern (Fig. 8a). The projected sea level timeseries of reanalysis onto the APT tripole pattern exhibits a high correlation (correlation = 0.67; p-value < 0.01) with the EOF3

timeseries (Fig. 8b vs Fig. 6f), suggesting that this predictable sea level component originates from the NA tripole mode. The prediction skill is then estimated by correlating the timeseries of the component in the hindcasts and satellite observation. The correlation coefficient displays that the NA tripole mode is predictable two years in advance (Fig. 8c). This two-years prediction skill is very likely related with the ocean circulation adjustment (e.g., Rossby wave propagation) associated with the NAO-driven NA tripole mode. At 32°–34°N, the Rossby wave takes about two years to propagate from 40°W to 60°W[40] (Supplementary Fig. 4), which can provide a multiyear prediction skill for the sea level along the USSEC.
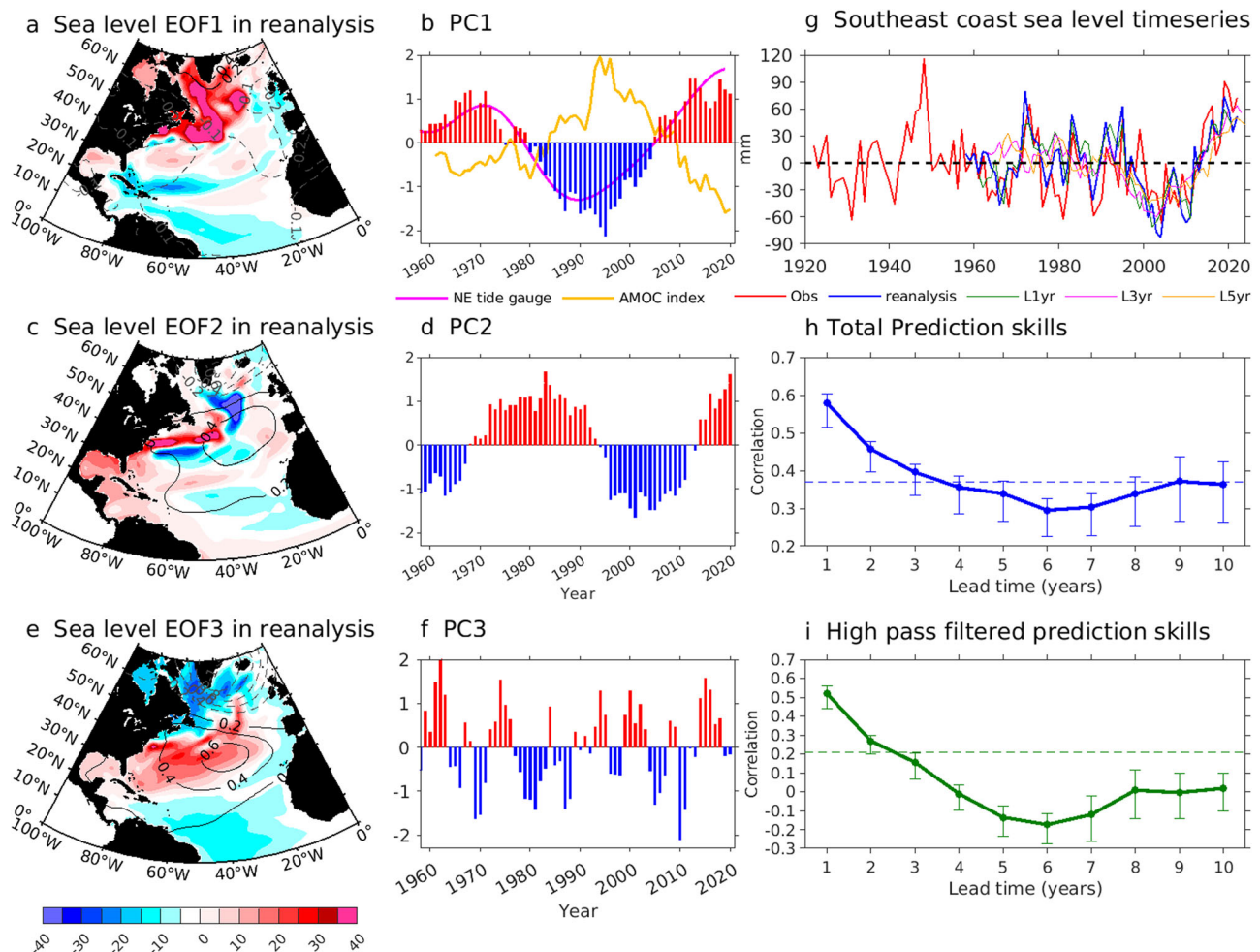
Fig. 6 | North Atlantic sea level variability going back into the 20th century. a The leading empirical orthogonal function (EOF1) of detrended sea level variability in 1958–2022 in the SPEAR reanalysis. Unit is mm. **b** The first principal component (PC1) of sea level in the SPEAR reanalysis (red and blue bars). The magenta line denotes the detrended and low-pass filtered (> = 15-year) sea level timeseries at the U.S. Northeast Coast Tide Gauge (TG) stations. The yellow line denotes the Atlantic meridional overturning circulation (AMOC) index in the SPEAR reanalysis, which is defined as the maximum streamfunction within 20°–60°N latitudinal band and below 500 m in depth space. All these timeseries are normalized by their respective standard deviations and thus the unit is 1. The contours in (a) are the sea level pressure regressions upon the PC1 time series. **c, d** Same as (**a, b**) but for the second EOF component of sea level. **e, f** Same as (**a, b**) but for the third EOF component of sea level. **g** The detrended sea level timeseries at TG stations along the U.S. Southeast Coast in 1920–2022 (red line) along with the detrended sea level timeseries in the SPEAR reanalysis (blue line) and initialized decadal hindcasts at a lead time of 1 year (green line), 3 years (magenta line) and 5 years (yellow line). **h** The anomaly correlation between the detrended ensemble mean sea level timeseries in the initialized decadal hindcasts and detrended TG observations in 1958–2022 as a function of lead times. The error bars around the line denote the ensemble spread at each lead time. The dashed line denotes the 90% confidence level using a Monte Carlo method. **i** Same as (**h**) but for the high-pass filtered (< 5 yr) sea level timeseries.

Discussion

In the present study, we investigated the potential physical drivers responsible for the observed acceleration of sea level rise (SLR) after 2010 along the U.S. Southeast Coast (USSEC). Additionally, we explored the multiyear predictability of sea level over the North Atlantic (NA) ocean and along the USSEC. These objectives are pivotal in climate science, particularly given the significance of rapid SLR for assessing coastal flood risk. We find that the accelerated SLR along the USSEC after 2010 represents the compounding effects of long-term global warming trend, multidecadal buoyancy-driven AMOC variations, and wind-driven oceanic response to interannual variations in the NAO. It's noteworthy that the multidecadal AMOC variations could also be externally influenced by the NAO[41,42]. It's important to highlight that our study does not aim to precisely distinguish between the forced signal and internal variability. Instead, our focus is on revealing potential physical drivers and sources of predictability.

Multiple lines of observational and modeling evidence suggest that the multidecadal NAO variations drive multidecadal AMOC variabilities

through changes of heat flux in the Labrador Sea[43]. This buoyancy-driven AMOC variability propagates southward with an interior advection speed, which is accompanied with a meridional shift of the GS path[34]. The associated heat transport anomalies lead to a SLR near the GS path and the USSEC in the most recent decade. Meanwhile, the observed short time scale NAO variations prompt a NA sea level tripole via wind driven circulation adjustments. This results in a widespread SLR across the entire subtropical band after 2010, adding to the effects of buoyancy-driven AMOC induced SLR.

Using a state-of-the-art decadal prediction system, we show that the sea level and its associated coastal flooding risk along the USSEC are potentially predictable on multiyear timescales. Our decadal hindcasts show that the AMOC (buoyancy-driven) induced changes in SLR are predictable 5 years in advance due to observationally based initialization of the AMOC in prediction system. In addition, the short time scale NAO variations generate a NA tripole mode of sea level that is predictable two years in advance. This predictability is very likely from a slow oceanic adjustment (e.g., the ocean Rossby wave) to atmospheric circulation changes, which in turn manifests
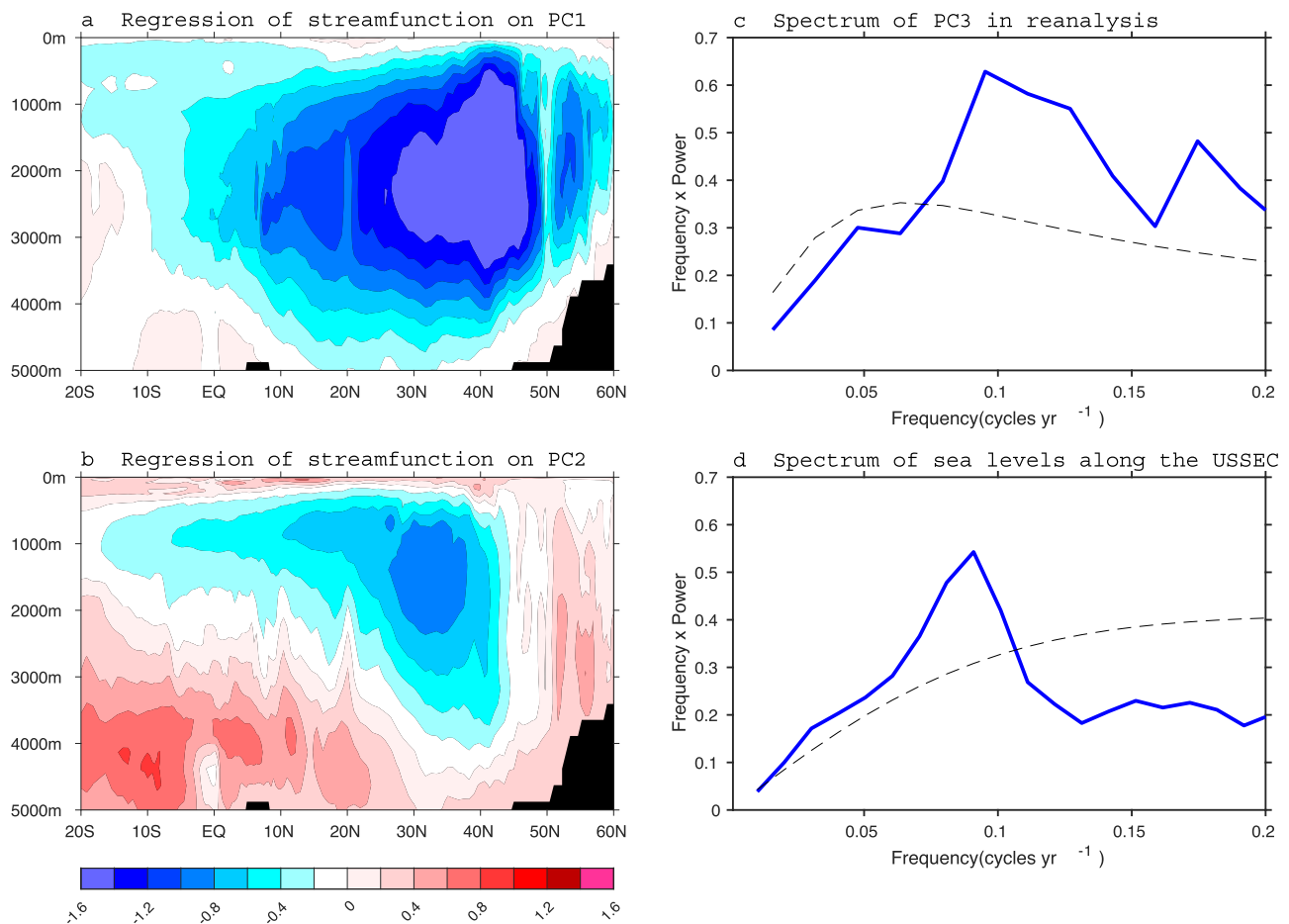
Fig. 7 | The Atlantic meridional overturning circulation (AMOC) states associated with the dominant modes of sea level in SPEAR reanalysis (1958–2022), and the power spectrum of sea level timeseries. a Regression of the Atlantic streamfunction (Sv) against the first principal component (PC1) of North Atlantic (NA) sea level (Fig. 6b) in reanalysis. **b** Same as (**a**) but for the streamfunction regression against the PC2 of NA sea level (Fig. 6d). **c** Power spectrum of the normalized timeseries of PC3 of the NA sea level in reanalysis (Fig. 6f). **d** Power spectrum of the normalized detrended sea level timeseries at the U.S. Southeast coast (USSEC) Tide Gauge stations (Fig. 6g).

in the prediction of coastal sea levels. Our forecasting system also indicates that the detrended sea level variability is anticipated to gradually decrease in the coming years (Fig. 9). This reduction is attributed to a weakening of the wind-driven NA tripole mode (Fig. 8b) and a slight decrease in sea level induced by the AMOC transition state (see Fig. 2f in our previous paper[36]). This indicates that the rapid SLR acceleration along the USSEC is very likely to slow down in the next five years.

This study is the first attempt to link the coastal sea level variabilities and predictabilities to both buoyancy-driven AMOC and wind-driven NA tripole mode. Our primarily focus is to underscore that the rapid SLR along the USSEC results from the cumulative impact of long-term global warming trend, buoyancy-driven AMOC variations, and an oceanic tripole-like response to NAO variations, rather than underscoring the sole importance of internal variability. We stress the challenge of accurately distinguishing the forced signal from internal variability in observations and models. External forcing may also contribute to the AMOC variability[41,42]. While acknowledging the inherent difficulty in achieving absolute accuracy in observations and models, our comprehensive analysis incorporating satellite, TG observation, and SPEAR models consistently aligns qualitatively. All identified phenomena and processes align with our physical understanding, significantly boosting confidence in our conclusions. Additionally, it's important to note that the SPEAR model used in this study has low ocean resolution and lacks incorporation of tide and land ice components. Furthermore, it cannot simulate non-climate factors such as the vertical land movement. Therefore, the relationships proposed here require validation

from other climate models and should be revisited as more observations and advanced climate models become available.

Methods
Observations
The sea level observations by altimetry satellites started in 1993 and have a near global coverage. Here, we use the monthly gridded sea surface height (SSH) with a quarter degree resolution, which is released by the Copernicus Marine and Environment Monitoring Service (CMEMS)[19]. We also use the monthly sea level observations at Tide Gauge (TG) stations since the 20th century processed and distributed by the Permanent Service for Mean Sea Level (PSMSL)[20]. We correct the inverted barometer (IB) effect in TG observations in order to be in agreement with the satellite datasets. The IB is defined as $IB = \frac{P_{l-} P_{gmean}}{\rho_0 g}$, where P_l is local sea level pressure (SLP), P_{gmean} is the global ocean averaged SLP, ρ_0 is the sea water density and g is gravity. The 55-year Japanese Reanalysis (JRA-55) SLP dataset[44] is used here to calculate IB.

Models
The fully coupled model used in the present study comes from the GFDL Seamless system for Prediction and Earth system Research (SPEAR)[30]. Here, we use the low ocean resolution version named SPEAR_LO. The ocean and ice components of SPEAR_LO are from MOM6[45], which has a ~ 1° horizontal resolution with refined 1/3° meridional resolution in the tropics and 75 hybrid ocean layers in the vertical. The atmosphere and land components

Fig. 8 | The predictable component of sea level in the SPEAR initialized decadal hindcasts/forecasts.
a The predictable component of sea level (mm) over the North Atlantic Ocean derived from the average predictability time (APT) method. **b** The ensemble mean (magenta line) and spread (pink shading) timeseries as a function of lead times for the decadal hindcasts initialized on 1 January every five years from 1961 to 2021. The red (blue) line is the time-series for projecting the SPEAR reanalysis (satellite observation) onto the APT component. **c** Anomaly correlation between the APT timeseries in hindcasts and projected satellite observation timeseries as a function of lead times (yellow solid line). The error bars around the line denote the ensemble spread at each lead time. The dashed black line denotes the 90% confidence level using a Monte Carlo method.
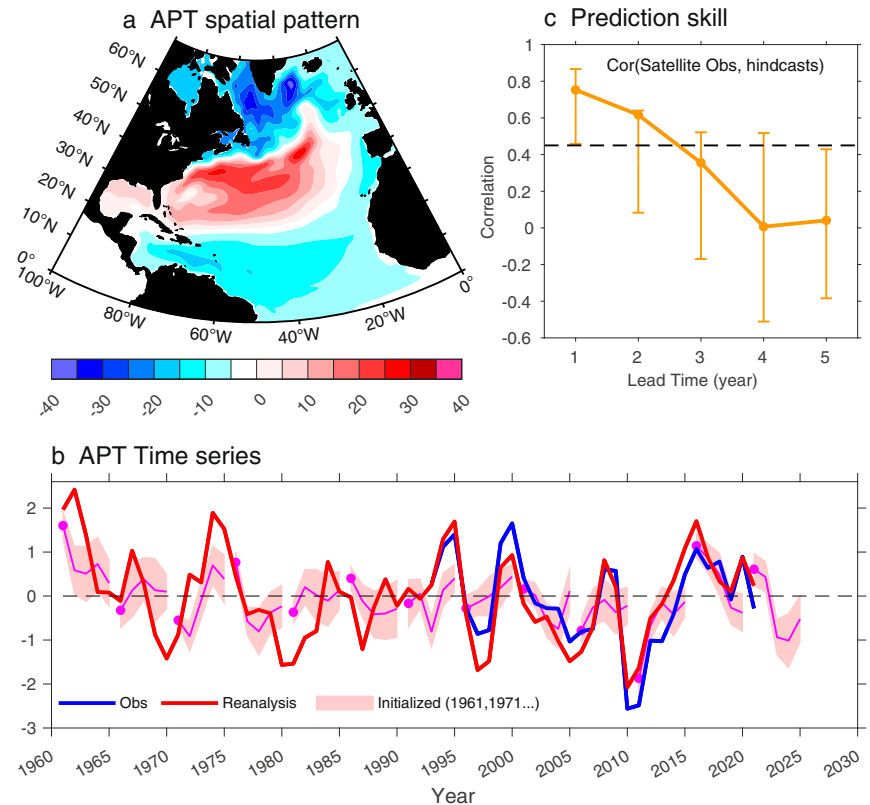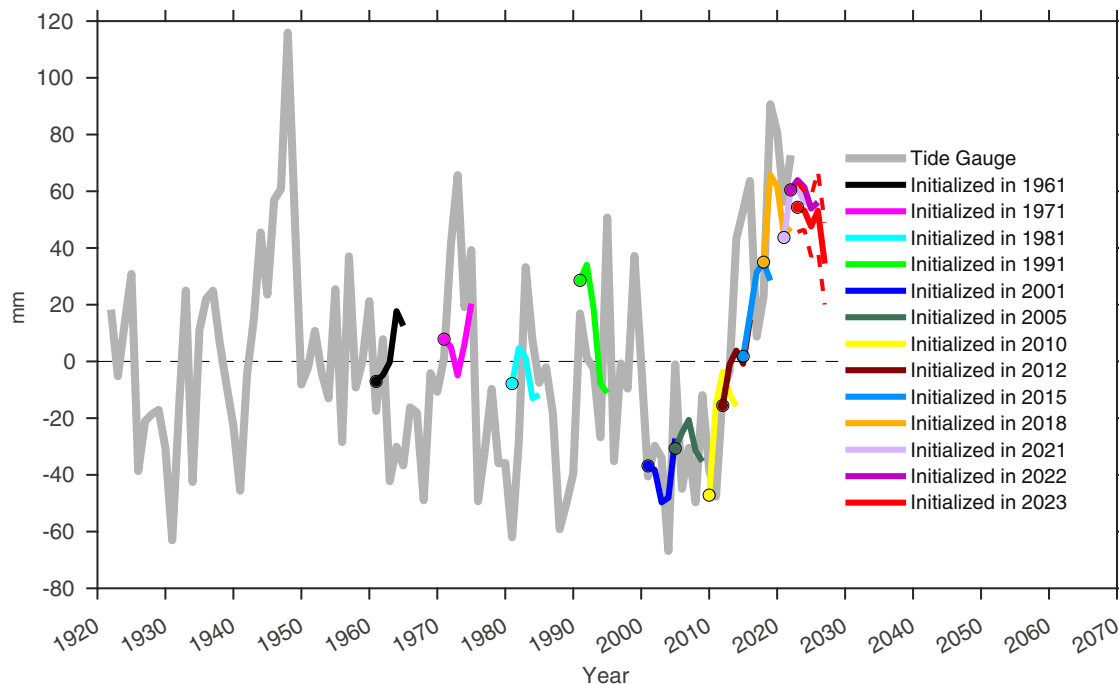

Fig. 9 | 5-year predictions of detrended sea level at different initialization years.
a The detrended annual mean sea level time series at U.S. Southeast tide gauge stations (thick gray lines) and ensemble mean predicted 5-year sea level trajectories initialized between 1961 and 2023 (solid color lines). The dashed red lines are the ensemble spread for the sea level prediction initialized in 2023 estimated by the one standard deviation of all members. Unit is mm.

of SPEAR_LO are from the AM4-LM4[46,47] with a ~ 100 km resolution in the horizontal and 33 levels in the vertical. We conduct a long-time integrating control simulation of SPEAR_LO, with atmospheric composition fixed at preindustrial 1850 concentrations.

We developed a SPEAR reanalysis for initializing retrospective decadal prediction system based on SPEAR_LO[21]. In SPEAR reanalysis, the atmospheric temperature and winds were restored toward the 55-year Japanese Reanalysis (JRA-55)[43] on a 6-hourly time scale and the

SST restoring within 60°S-60°N was confined to the Extended Reconstructed Sea Surface Temperature version 5 (ERSSTv5)[48]. Due to atmosphere and SST constraints, the ocean component in reanalysis experiences a sequence of quasi-observation boundary conditions which then drive multidecadal AMOC evolutions in the reanalysis (Supplementary Fig. 5). The AMOC multidecadal variability in SPEAR reanalysis is largely buoyancy driven, which is associated with the heat flux changes in the Labrador Sea because of the observed low frequency NAO variations[43]. The AMOC timeseries at 26.5°N in reanalysis is highly correlated with the RAPID array observation with a correlation coefficient of 0.59 (p-value < 0.05) (Supplementary Fig. 5), which largely enhances our confidence on the SPEAR reanalysis. The retrospective decadal prediction system based on the SPEAR_LO were then initialized from the SPEAR reanalysis. The hindcasts/forecasts have 20 ensemble members, and each member was initialized on 1 January every year from 1961 to 2022 from different members of reanalysis. The hindcasts/forecasts were integrated for 10 years with the realistic time evolving radiative forcings. To remove the systematic model drift, we subtract the lead-time-dependent climatology from hindcasts/forecasts before analysis.

Monte Carlo method. In the present paper, we use a Monte Carlo method to test the significance of correlation coefficient of two timeseries. We begin by computing the correlation coefficient between the two timeseries (referred to as observed correlation). Following this, we generate a large number of surrogate datasets by shuffling one of the time series while keeping the other fixed. For each randomly generated dataset, we calculate the correlation coefficient between the two timeseries. Subsequently, we construct the sampling distribution by plotting the kernel density estimate of the correlation coefficients obtained from the surrogate datasets. The p-value is then computed by determining the proportion of surrogate correlations that are greater than or equal to the observed correlation. If the p-value falls below a predetermined significance threshold (e.g., 0.1), we reject the null hypothesis and conclude that there is a significant correlation between the two timeseries.

Linear detrending of datasets. For the satellite observation, we employ linear detrending at each grid prior to EOF analysis. The exclusion of external forcing cannot be guaranteed in the detrended sea level timeseries. This is because each method, whether it's linear detrending, removing global mean sea level, eliminating the first EOF component of sea level, or removing the ensemble mean/first signal-to-noise EOF[49,50] from SPEAR large ensemble simulations, has its own drawbacks. Removing a global mean does not account for regional impacts of external forcing such as on the NAO. Linearly detrending and eliminating the first EOF does not account for short term external forcing for example from aerosols, volcanoes, and solar variations. Removing a large ensemble mean will reveal modelled internal variability but the real word could be very different. It's crucial to emphasize that in our current study, our aim is not to precisely separate the forced signal from internal variability, but rather to identify physical drivers and potential sources of predictability.

For Tide Gauge (TG) station sea level observations, we also employ a straightforward linear detrending before analysis. This choice is influenced by the extended duration of TG observations, which only cover specific points. Since long-term global sea level observations are unavailable, methods such as removing global mean sea level and the first EOF component are impractical. Additionally, the absence of a land ice component in climate models rules out the use of large ensemble simulations. Moreover, a notable characteristic in TG observations is the discernible linear trend in the total sea level time series at U.S. East Coast stations. This trend supports the rationale for employing linear detrending as a suitable method for removing global warming trend. To align satellite and TG observations, we apply linear detrending to the datasets before analysis, as needed, in both the SPEAR reanalysis and initialized decadal prediction system.

Steric and thermosteric/halosteric sea level

The steric sea level is calculated by integrating the in-situ density anomaly (ρ') with respective to the time mean over the entire vertical levels and has a form of $-\frac{\int \rho'(T,S,z)dz}{\rho_0}$, where ρ_0 is the averaged sea water density (1027.5 kg m^{-3}), T is temperature, S is salinity and z is ocean depth. T and S are functions of time and location. The thermosteric (halosteric) sea level is calculated similarly, but we use the time mean salinity (temperature) to get the density anomalies. Thus, the thermosteric (halosteric) sea level has a form of $-\frac{\int \rho'(T,\bar{S},z)dz}{\rho_0}$ ($-\frac{\int \rho'(\bar{T},S,z)dz}{\rho_0}$).

Thermosteric sea level equation

The thermosteric sea level (SL_{thermo}) variability is associated with the temperature advection by ocean current and the net surface heat flux[13,26]:

$$\frac{\partial SL_{thermo}}{\partial t} = -\alpha \int_{-H}^{0} \mathbf{u} \bullet \nabla T dz + \alpha \frac{Q_{net}}{\rho_0 C_p},$$

where α is thermal expansion coefficient, $\mathbf{u}$ is ocean current velocity, T is ocean temperature, z is ocean depth, H is the depth of ocean bottom, ρ_0 is sea water density, C_p is the specific heat capacity of sea water and Q_{net} is the net surface heat flux (positive downward). When we integrate the sea level equation within an area A (e.g., subtropical gyre region) and the surface heat flux contribution is small, the sea level equation is then approximately as $\frac{\partial SL_{thermo}}{\partial t} \approx \alpha \frac{\Delta MHT}{\rho_0 C_p A}$, where $\Delta MHT = MHT_{low\_latitude} - MHT_{high\_latitude}$ denotes the meridional heat transport difference between the low latitude and high latitude. The positive (negative) value of ΔMHT means meridional heat transport convergence (divergence), which favors a warming (cooling) and therefore an uplift/a low of sea level.

APT method

The average predictability time (APT) method[37,38] is used to identify the most predictable components of sea level in the SPEAR decadal prediction system. The APT is defined as twice the integral of predictability over all lead times:

$$APT = 2 \sum_{\tau=1}^{\infty} \left(1 - \frac{\delta_\tau^2}{\delta_\infty^2} \right),$$

where δ_τ^2 is ensemble forecast variance at a lead time of τ and δ_∞^2 is climatological variance. Maximizing APT leads to an eigenvalue problem. Thus, the APT analysis is very similar to the EOF analysis, but we decompose the predictability here instead of variance. The Monte Carlo approach is used to test the statistical significance of APT. In the current study, we use the integral of sea level predictability over 1–5 lead years. The leading three predictable components correspond to the external radiative forcing, the AMOC mature and transition phases, respectively, as shown in our previous paper[36]. The fourth predictable component is associated with the NA sea level tripole mode, which is statistically significant and exhibited in the present paper.

Data availability

The Data and Services Center (AVISO) observed sea surface height (SSH) is available at https://marine.copernicus.eu/access-data. The sea level timeseries from tide gauge stations is available at the Permanent Service for Mean Sea Level https://psmsl.org. The data for figures are available online at https://doi.org/10.5281/zenodo.10810696.

Code availability

The source code of ocean component MOM6 of SPEAR_LO model is available at https://github.com/NOAA-GFDL/MOM6.

References

1. Fitzgerald, D. M., Fenster, M. S., Argow, B. A. & Buynevich, I. V. Coastal impacts due to sea-level rise. *Annu. Rev. Earth Planet. Sci.* **36**, 601–647 (2008).
2. Hinkel, J. et al. Coastal flood damage and adaptation coasts under 21st-century sea level rise. *Proc. Natl. Acad. Sci.* **111**, 3292–3297 (2014).
3. Woodruff, J., Irish, J. & Camargo, S. Coastal flooding by tropical cyclones and sea-level rise. *Nature* **504**, 44–52 (2013).
4. Ezer, T. & Atkinson, L. P. Accelerated flooding along the US East Coast: On the impact of sea-level rise, tides, storms, the Gulf Stream, and the North Atlantic Oscillations. *Earth's Future* **2**, 362–382 (2014).
5. Rahmstorf, S. Rising hazard of storm-surge flooding. *Proc. Natl. Acad. Sci. USA* **114**, 11806–11808 (2017).
6. Yin, J., Griffies, S. M., Winton, M., Zhao, M. & Zanna, L. Response of storm related extreme sea level along the US Atlantic coast to combined weather and climate forcing. *J. Clim.* **33**, 3745–3769 (2020).
7. Piecuch, C. G. et al. How is New England Coastal Sea Level Related to the Atlantic Meridional Overturning Circulation at 26°N? *Geophys. Res. Lett.* **46**, 5351–5260 (2019).
8. Ezer, T. Detecting changes in the transport of the Gulf Stream and the Atlantic overturning circulation from coastal sea level data: The extreme decline in 2009–2010 and estimated variations for 1935–2012. *Glob. Planet. Change* **129**, 23–36 (2015).
9. Tebaldi, C. et al. Extreme sea levels at different global warming levels. *Nat. Clim. Change* **11**, 746–751 (2021).
10. Wdowinski, S., Bray, R., Kirtman, B. P. & Wu, Z. Increasing flooding hazard in coastal communities due to rising sea level: Case study of Miami Beach. Florida. *Ocean Coast. Manag.* **126**, 1–8 (2016).
11. Sweet, W., Dusek, G., Obeysekera, J. & Marra, J. Patterns and projections of high tide flooding along the U.S. coastline using a common impact threshold. NOAA Technical Report NOS CO-OPS, 86, National Oceanic and Atmospheric Administration, Silver Spring, 395 Maryland, USA (2018).
12. Dangendorf, S. et al. Acceleration of U.S. Southeast and Gulf coast sea-level rise amplified by internal climate variability. *Nat. Commun.* **14**, 1935 (2023).
13. Volkov, D. L., Lee, S.-K., Dominngues, R., Zhang, H. & Goes, M. Interannual sea level variability along the southeastern seaboard of the United States in relation to the Gyre-Scale heat divergence in the North Atlantic. *Geophys. Res. Lett.* **46**, 7481–7490 (2019).
14. Yin, J. Rapid decadal acceleration of sea level rise along the U.S. East and Gulf Coasts during 2010-2022 and its impact on hurricane-induced storm surge. *J. Clim.* **36**, 4511–4529 (2023).
15. Domingues, R., Goni, G., Baringer, M. & Volkov, D. What caused the accelerated sea level changes along the U.S. East Coast during 2010–2015? *Geophys. Res. Lett.* **45**, 13,367–13,376 (2018).
16. Valle-Levinson, A., Dutton, A. & Martin, J. B. Spatial and temporal variability of sea level rise hot spots over the eastern United States. *Geophys. Res. Lett.* **44**, 7876–7882 (2017).
17. Wdowinski, S., Bray, R., Kirtman, B. P. & Wu, Z. Increasing flooding hazard in coastal communities due to rising sea level: Case study of Miami Beach. *Fla. Ocean Coast. Manag.* **126**, 1–8 (2016).
18. Ezer, T. 2019: Regional differences in sea level rise between the Mid-Atlantic Bight and the South Atlantic Bight: Is the Gulf Stream to blame? *Earth's Future* **7**, 771–783 (2019).
19. Taburet, G. et al. DUACS DT2018: 25 years of reprocessed sea level altimetry products. *Ocean Sci.* **15**, 1207–1224 (2019).
20. Caldwell, P., Merrifield, M. & Thompson, P. Sea level measured by tide gauges from global oceans—The Joint Archive for sea level holdings, version 5.5. NOAA/National Centers for Environmental Information, accessed October 2018, https://doi.org/10.7289/v5v40s7w (2015).
21. Yang, X., et al. On the development of GFDL's decadal prediction system: Initialization approaches and retrospective forecast assessment. *J. Adv. Modeling Earth Syst.* **13**, https://doi.org/10.1029/2021MS002529 (2021).
22. Yin, J., Schlesinger, M. E. & Stouffer, R. J. Model projections of rapid sea-level rise on the northeast coast of the United States. *Nat. Geosci.* **2**, 262 (2009).
23. Sallenger, A. H., Doran, K. S. & Howd, P. A. Hotspot of accelerated sea-level rise on the Atlantic coast of North America. *Nat. Clim. Change* **2**, 884 (2012).
24. Meehl, G. A. et al. How much more global warming and sea level rise? *Science* **307**, 1769–1772 (2005).
25. Edwards, T. L. et al. Projected land ice contributions to twenty-first-century sea level rise. *Nature* **593**, 74–82 (2021).
26. Volkov, D. L. et al. Atlantic meridional overturning circulation increases flood risk along the United States southeast coast. *Nat. Commun.* **14**, 5059 (2023).
27. Cunningham, S. A. et al. Atlantic meridional overturning circulation slowdown cooled the subtropical ocean. *Geophys. Res. Lett.* **40**, 6202–6207 (2013).
28. Zhao, J. & Johns, W. Wind-forced interannual variability of the Atlantic Meridional Overturning Circulation at 26.5 N. *J. Geophys. Res. Oceans* **119**, 2403–2419 (2014).
29. Zhang, R. Coherent surface-subsurface fingerprint of the Atlantic meridional overturning circulation. *Geophys. Res. Lett.* **35**, L20705 (2008).
30. Delworth, T. L. et al. SPEAR – the next generation GFDL modeling system for seasonal to multidecadal prediction and projection. *J. Adv. Modeling Earth Syst.* **12**, https://doi.org/10.1029/2019MS001895 (2020).
31. Deser, C. & Timlin, M. S. Atmosphere–ocean interaction on weekly timescales in the North Atlantic and Pacific. *J. Clim.* **10**, 393–408 (1997).
32. Schneider, E. K. & Fan, M. Observed decadal North Atlantic tripole SST variability: II. Diagnosis of mechanisms. *J. Atmos. Sci.* **69**, 51–64 (2012).
33. Wu, L., He, F., Liu, Z. & Li, C. Atmospheric teleconnections of tropical Atlantic variability: Interhemispheric, tropical–extratropical, and cross-basin interactions. *J. Clim.* **20**, 856–870 (2007).
34. Zhang, R. Latitudinal dependence of Atlantic meridional overturning circulation (AMOC) variations. *Geophys. Res. Lett.* **37**, L16703 (2010).
35. Zhang, J. & Zhang, R. On the evolution of Atlantic Meridional Overturning Circulation Fingerprint and implications for decadal predictability in the North Atlantic. *Geophys. Res. Lett.* **42**, 5419–5426 (2015).
36. Zhang, L., Delworth, T. L., Yang, X. & Zeng, F. Skillful multiyear to decadal predictions of sea level in the North Atlantic Ocean and U.S. East Coast. *Commun. earth Environ.* **4**, 420 (2023).
37. DelSole, T. & Tippett, M. K. Average predictability time. Part I: Theory. *J. Atmos. Sci.* **66**, 1172–1187 (2009).
38. DelSole, T. & Tippett, M. K. Average predictability time. Part II: Seamless diagnosis of predictability on multiple time scales. *J. Atmos. Sci.* **66**, 1188–1204 (2009).
39. Zhang, L., Delworth, T. L. & Jia, L. Diagnosis of decadal predictability of Southern Ocean Sea surface temperature in the GFDL CM2.1 model. *J. Clim.* **30**, 6309–6328 (2017).
40. Zhang, H. & Wu, L. Predicting North Atlantic sea surface temperature variability on the basis of the first-mode baroclinic Rossby wave model. *J. Geophys. Res. Oceans* **115**, C09030 (2010).
41. Klavans, J. M., Cane, M. A., Clement, A. C. & Murphy, L. N. NAO predictability from external forcing in the late 20th century. *npj Clim. Atmos. Sci.* **4**, 22 (2021).
42. Liu, F. et al. Increased Asian aerosols drive a slowdown of Atlantic meridional overturning circulation. *Nat. Commun.* **15**, 18 (2024).
43. Delworth, T. L. et al. The North Atlantic Oscillation as a driver of rapid climate change in the Northern Hemisphere. *Nat. Geosci.* **9**, 509–513 (2016).

44. Kobayashi, S. et al. The JRA-55 Reanalysis: General specifications and basic characteristics. *J. Meteorol. Soc. Jpn.* **93**, 5–48 (2015).
45. Adcroft, A. et al. The GFDL global ocean and sea ice model OM4.0: Model description and simulation features. *J. Adv. Modeling Earth Syst.* **11**, 3167–3211 (2019).
46. Zhao, M. et al. The GFDL Global atmosphere and land model AM4.0/LM4.0: 1. Simulation characteristics with prescribed SSTs. *J. Adv. Modeling Earth Syst.* **10**, 691–734 (2018).
47. Zhao, M. et al. The GFDL Global atmosphere and land model AM4.0/LM4.0: 2. Model description, sensitivity studies, and tuning strategies. *J. Adv. Modeling Earth Syst.* **10**, 735–769 (2018).
48. Huang, B. et al. Extended Reconstructed Sea Surface Temperature, Version 5 (ERSSTv5): Upgrades, validations, and intercomparisons. *J. Clim.* **30**, 8179–8205 (2017).
49. Ting, M., Kushnir, Y., Seager, R. & Li, C. Forced and Internal Twentieth-Century SST Trends in the North Atlantic. *J. Clim.* **22**, 1469–1481 (2009).
50. Ting, M., Kushnir, Y., Seager, R. & Li, C. Robust features of Atlantic multidecadal variability and its climate impacts. *Geophys. Res. Lett.* **38**, L17705 (2011).

Acknowledgements

Author contributions

L.Z. conceived the initial idea, designed the study, performed the analysis, and wrote the manuscript. T.L.D., X.Y., F.Z., and L.Z. lead the development of SPEAR decadal prediction system. Q.G. and S.L. contributed to the interpreting the results and providing feedbacks. All authors contributed to the improvement of the manuscript.

Competing interests

The authors declare no competing interests.

Additional information

Publisher's note Springer Nature remains neutral with regard to jurisdictional claims in published maps and institutional affiliations.